

Z. MOKTADIR, Southampton University, UK

DOI: 10.1533/9780857099334.3.341

Abstract: The use of graphene in the development of nanoscale mechanical structures is reviewed. The recent development of graphene resonators and techniques used to fabricate and characterise them is described. Some applications in sensor technology are highlighted.

Key words: graphene, mechanical resonators, nanoelectromechanics, sensors.

14.1 Introduction

Despite being a single atomic layer, graphene is one of the strongest materials, stronger than steel (Lee *et al.*, 2008); that is, it has a strong ability to survive failure under large applied load. Moreover, graphene is a very flexible material and impermeable to gases (Bunch *et al.*, 2008) making it suitable for a variety of applications including life sciences. It is therefore obvious to consider graphene as a material with good mechanical properties for applications in nanomicroelectromechanical systems (NEMS/MEMS). Such applications might range from sensing to actuation or applications in biotechnology (Wu *et al.*, 2009, Alwarappan *et al.*, 2009). By combining electronic and mechanical properties of graphene, devices with enhanced functionality can be fabricated.

Atoms in a single atomic-layer graphene sheet are arranged in a honeycomb structure and are bonded in a sp^2 configuration with a carbon–carbon bond length of about 1.42 Å. Single layer graphene sheets can be stacked together to form multilayer graphene with the interlayer distance of 3.35 Å (Delhaes, 2001). Studies with scanning electron microscope showed that graphene ripples. It is still debatable whether these ripples are intrinsic or extrinsic (Fasolino *et al.*, 2007, Ishigami *et al.*, 2007). They could be caused either by impurities or by the underlying substrate. Despite this, graphene seems to preserve its remarkable mechanical attributes compared with other materials. We shall see in the subsequent sections how these attributes can be explored to develop enhanced nanomechanical systems.

Chapter 14 is organised as follows: in 14.2, we draw a comparison between two outstanding materials, graphene and silicon; in 14.3, we detail graphene's mechanical parameters, including Young modulus and Poisson ratio; fabrication methodologies and problems are addressed in 14.4; in 14.5, we

explore graphene resonant nanostructures; in 14.6, we present examples of nanomechanical sensing devices made with graphene; and, in 14.7, we discuss future trends for graphene nanodevices.

14.2 Graphene versus silicon

It is instructive to compare graphene with one of the outstanding materials for MEMS and NEMS, i.e. single-crystal silicon. Silicon has dominated MEMS technology for the last two decades, allowing this technology to generate a market worth billions of dollars (Yole, <http://www.yole.fr/Reports.aspx>). Considering the remarkable potential of graphene, it is anticipated that this material has the potential to contribute to MEMS and NEMS technologies and even compete with silicon at the same level. In Table 14.1, a comparison between the two materials is shown, in terms of some of their material parameters. One notices for instance, that graphene has a higher Young modulus than silicon, allowing the fabrication of high-frequency resonators from graphene. For example, a nanobeam made of multilayer graphene has a resonant frequency roughly three times larger than that of a beam of silicon having the same dimensions, according to values listed in Table 14.1.

The remarkably higher thermal conductivity and high current carrying capacity allows the use of graphene as interconnects in electronic chips, potentially replacing copper. The high values of graphene mobility provides a good material for use as a channel in metal oxide semiconductor field effect transistors (MOSFETs). Thin-body silicon has emerged as one of the promising materials for NEMS, and for the development of novel silicon-based high-speed devices, as well as offering high-density integration. Devices made of thin silicon-on-insulator (SOI) use the hybrid approach i.e. a combination of moveable structures and MOSFETs on the same platform (Abele *et al.* 2005, Buks and Roukes 2001, Garcia-Ramirez *et al.* 2010, Tsuchiya *et al.* 2005). In principal, this hybrid approach can be simplified even more in graphene, because the moveable structure is graphene itself, which can be electronically gated and, therefore, used as a sensor without the need for a side transistor. Graphene is mainly produced using the three following methods: mechanical exfoliation of graphite (Novoselov *et al.*, 2004, 2005); epitaxial growth on SiC (Emtsev *et al.*, 2009, de Heer *et al.*, 2007); and chemical vapour deposition (CVD) onto metallic foil (Cu, Fe and other transition metals) (Kim *et al.*, 2009, Li *et al.*, 2009a, b, Obraztsov *et al.*, 2007). Thin graphitic layers can be epitaxially grown on 4HSiC substrate by the thermal decomposition of either Si- or C-terminated surface species. The main advantage of epitaxial graphene on silicon carbide is the possibility of large-area patterning using standard microelectronics processes; for instance, large-area integration of electronics on the wafer

Table 14.1 Silicon and graphene material parameters

	Young modulus (TPa)	Electron mobility (cm ² V ⁻¹ s ⁻¹)	Thermal conductivity (W m ⁻¹ K ⁻¹)	Poisson ratio
Graphene	~1 (Lee <i>et al.</i> , 2008)	>15000 (Novoselov <i>et al.</i> , 2005)	~5000 (Balandin <i>et al.</i> , 2008)	~-0.165 (Lee <i>et al.</i> , 2008)
Silicon	~0.13 (Dual <i>et al.</i> , 1997)	<1400 (Norton <i>et al.</i> , 1973)	~1500 (Gad-el-Hak, 2002)	~-0.28 (Gad-el-Hak, 2002)

scale is possible (Hass *et al.*, 2006). Exfoliation of graphene sheets remains the only method that produces high-quality graphene flakes, obtained by micromechanical cleavage of bulk graphite. Graphene can benefit from the mature IC technologies developed for silicon although the bottom-up approach is also a viable route towards graphene MEMS/NEMS.

14.3 Graphene mechanical attributes

Since the discovery of graphene, several experiments have been performed to measure the Young modulus, strength and the Poisson ratio of graphene atomic sheets. In this section, we discuss the experimental methods used to measure these parameters.

14.3.1 Young modulus

In linear materials (obeying Hook's law), the Young modulus E is defined as the ratio of the tensile stress to the tensile strain and, in an isotropic elastic material, this is given by:

$$\sigma = E\varepsilon \quad [14.1]$$

where ε is the uniaxial strain. Experimentally, the Young modulus is determined by tensile stress tests experiments: a load is applied to the specimen in one direction and the resulting displacement is measured; the Young modulus is given by the gradient of the load–displacement plot. In silicon MEMS and NEMS, as we are dealing with sizes from a few tens of micrometres down to a few tens of nanometres, in general, several *on-chip* experimental tensile test setups were developed (Sato *et al.*, 1998, Tsuchiya *et al.*, 2005). Atomic force microscopy (AFM) is also extensively used as a

measurement technique, mainly for nanometre-sized specimens (Tanaka *et al.*, 2004, Wong *et al.*, 1997). These on-chip measurements allowed the characterisation of a wide variety of materials including MEMS components (Sato *et al.*, 1998) made on single-crystal silicon, carbon nanotubes (Yu *et al.*, 2000) and nanowires (Marszalek *et al.*, 2000).

The elastic parameters are a function of elastic constants that constitute the elements of the stiffness tensor relating the stress and strain tensors. For monolayer graphene, these parameters are for a two-dimensional material, so that the units used for stress are in Nm^{-1} . In a recent development, Lee *et al.* (2008) used AFM nanoindentation to determine elastic parameters of monolayer graphene membranes suspended over open holes. These experiments used exfoliated graphene on a pre-patterned silicon oxide substrate. The measured force–displacement graph is described by the expression:

$$F = \sigma_0(\pi r) \left(\frac{\delta}{r} \right) + E(q^3 r) \left(\frac{\delta}{r} \right)^3 \quad [14.2]$$

where δ is the displacement, r is the radius of the suspended membranes, σ_0 is the pretension, E the Young modulus and q is related to the Poisson ratio ν by $q = 1/(1.049 - 0.15\nu - 0.16\nu^2)$. The fit of the experimental data to equation [14.2] allowed the determination of the Young modulus $E \cong 342 \text{ Nm}^{-1}$. This gives a value of the effective Young modulus (dividing E by the graphite interlayer distance $\approx 0.335 \text{ nm}$) of 1TPa.

In other related work, Bunch *et al.* (2007) measured the Young modulus of suspended graphene beams and cantilevers over SiO_2 trenches. They used electrostatic as well as optical actuation to measure the resonance frequency of the suspended sheets. The thickness of their structures varied from the thickness of a single-layer graphene to a few nanometres. Within experimental uncertainty, they found values of the Young modulus between 0.5 and 2TPa. These values were obtained by fitting the theoretical expression for the resonance frequency with the measured values. The values found for the Young modulus are higher than those of silicon resonators made on SOI, but very close to those of carbon nanotubes (Qian *et al.*, 2002).

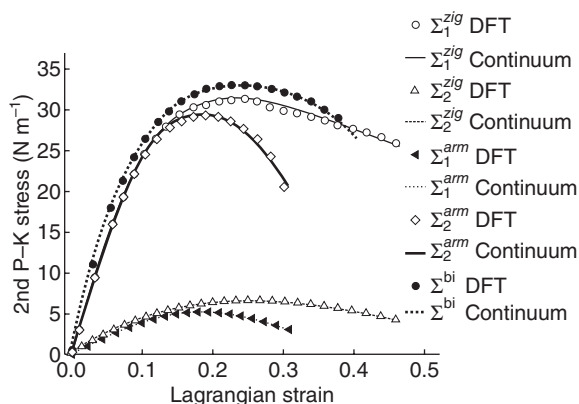
14.3.2 Poisson ratio

In most cases, the values of Poisson ratio for graphene were set to 0.16, which corresponds to graphite in the basal plane (Blakslee *et al.*, 1970). This is supported by a significant body of theoretical work using first-principal calculations (Liu *et al.*, 2007) or molecular dynamics (Jiang *et al.*, 2009), as well as continuum theories (Atalaya *et al.*, 2008, Cadelano *et al.*, 2009). Wei *et al.* (2009) performed *ab initio* calculations (using density functional

theory) on monolayer graphene from which they derived the nonlinear elastic constants appearing in the second-order elastic tensor. In Fig. 14.1, the strain–stress curve resulting from *ab initio* calculations is shown as well as the fit to the continuum nonlinear theory. The continuum description and the *ab initio* calculations showed excellent agreement. The derived Poisson ratio was 0.17. *Ab initio* calculations of Liu *et al.* (2007) gave a Poisson ratio of 0.186 at small strain, very close to the value of Wei and co-workers. At large strain, the Poisson ratio becomes anisotropic and determines whether the strain is in the *zigzag* direction or the *armchair* direction.

14.3.3 Mechanical strength

The first experimental determination of the breaking strength of monolayer graphene was by Lee *et al.* (2008). In their study, suspended monolayer graphene was brought to failure under a maximum strain using indentation with an AFM tip. The value of the breaking strength was 42 N m^{-1} for a defect-free graphene. These experiments showed that the breaking force depends only on the radius of the tips used for indentation and not on the size of the suspended membranes. This value is very close to that predicted from first principles. Liu *et al.* (2008) performed *ab initio* calculations to derive the breaking strength in an ideal graphene sheet in two different directions: the *zigzag* and *armchair* directions (under uniaxial strain). Their



14.1 Stress–strain *ab initio* calculation for uniaxial strain in armchair and zigzag directions and equibiaxial strain. Different lines correspond to different stress tensors. For example Σ_1^{arm} indicates the first component in the second P–K stress tensor under uniaxial strain in the armchair direction. Symbols correspond to the second P–K stress and Lagrangian strain data from *ab initio* calculations and continuous curves to least-squares fit results are plotted as solid lines. (From Wei *et al.*, 2009, with permission.)

main finding is that the breaking strength is anisotropic and has a value of 40.4 N m^{-1} in the armchair direction and a value of 36.7 N m^{-1} in the zigzag direction.

14.4 Fabrication technology for graphene microelectromechanical systems (MEMS)

There are a variety of technologies used to pattern and fabricate graphene nanodevices, depending on the application sought. We can learn a great deal from the mature MEMS top-down technologies and fabrication techniques developed for silicon. This allows ready integration of graphene with existing materials for MEMS and NEMS. For example, graphene can be sandwiched between different layers and contacted through vias in 3D multichip design, allowing the integration of mechanical and electronic components (Kim *et al.*, 2011). Because, graphene is chemically inert, it can be used with a variety of etchants. There is the potential of integration of graphene with silicon (Kim *et al.*, 2011); however, large-scale production of graphene is required to achieve this. Currently, the only viable option for this is the transfer of graphene grown by chemical vapour deposition (CVD), to another substrate (see for example Lee *et al.*, 2010). However, transferred graphene still suffers from a high density of defects (Huang *et al.*, 2011).

14.4.1 Wet and dry etching

To fabricate a graphene device, a combination of different processes is used, *viz* film deposition, lithography and etching. Thin film deposition is used to protect graphene layers or to define gate oxides in graphene field-effect devices. Examples of such materials are hafnium oxide (HfO_2), alumina (Al_2O_3) and silicon oxide (SiO_2). Metallic films deposition is used to define contact leads as well as contact pads (e.g. Au, Ti, Pd and Cr). Magnetic materials are used as source and drain contacts in graphene spin devices. Thin films are deposited either by thermal evaporation, sputtering, chemical vapour or atomic layer deposition. Patterning of graphene generally uses the following three major lithographic techniques: photolithography, electron beam (ebeam) lithography and direct write with a focused-ion beam. Photolithography is used to pattern features larger than a micrometre, for example in the fabrication of graphene MEMS resonators. Ebeam lithography is used to pattern sub-micron features such as graphene nanoribbons, quantum dots or a submicrometre channel in a FET transistor. A variety of photoresists such as S1813 is used in photolithography. Bilayer poly(methyl methacrylate) PMMA/MMA resists is widely used in ebeam lithography, mainly to define electrical contacts or submicrometre patterning of graphene. Nanoimprint lithography can also be used for graphene

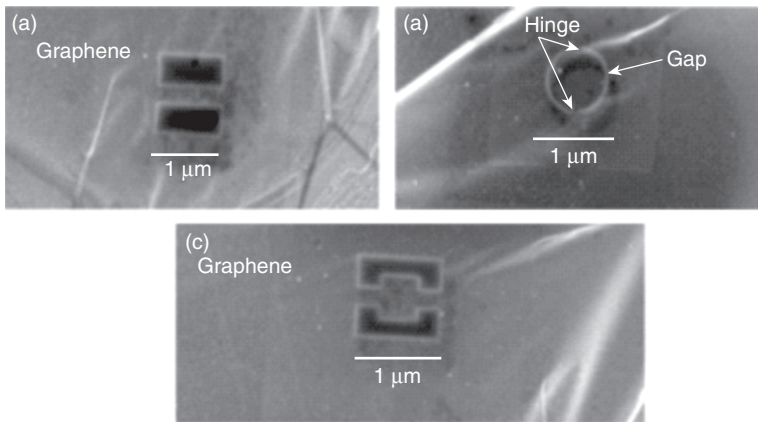
patterning (Wang *et al.*, 2011). As a carbon based material, graphene can be easily etched with oxygen plasma. This is the most widely used dry etching method where a hard or a resist mask is employed, although controlling under-etching during the definition of graphene nanoribbons a few 10s of nanometres in width is still challenging. Subsequently, resist masks are removed with acetone and isopropanol (IPA). Annealing of graphene samples is often required after resist stripping, as the resist residue always remains on the graphene surface. This residue can have a detrimental effect on the performance of graphene devices, mainly when probing the intrinsic properties of graphene. A recent study (Lin *et al.*, 2012) using transmission electron microscopy (TEM) and Raman spectroscopy has shown that the physisorbed PMMA cannot entirely be removed after annealing at workable temperatures for graphene (around 300°C in a H₂/Ar atmosphere). Therefore, new resists have to be tried and new cleaning methods need to be developed for graphene to reclaim its pristine condition after processing.

Although wet etchants are not generally used to pattern graphene, they are used to etch materials adjacent to it. For instance, buffered hydrofluoric acid (BHF) is used to suspend graphene beams and membranes by etching away the underlying oxide without attacking the graphene (Meyer *et al.*, 2007). So far, no systematic study concerning the behaviour of graphene in wet etchants was carried out. It is essential for compatibility that such a study is undertaken in order to integrate graphene with existing MEMS and NEMS processes and materials.

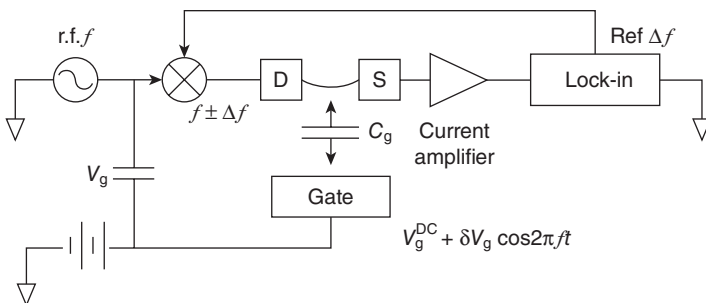
14.4.2 Focused-ion beam

Focused-ion beam (FIB) technology is used as a tool for analysis, selective deposition and sputtering of materials (Reyntjens and Puers, 2001). In the FIB method, a focused-ion beam is directed towards the target material causing its sputtering. The ion mainly used in commercial systems is the gallium ion. A recent commercially available FIB system is the helium ion microscope (HIM) which uses a helium focused on beam instead of gallium (Boden *et al.*, 2010). Gallium ion FIB can be used to exfoliate graphite to obtain a few layers of graphene (Lee *et al.*, 2010) and for nanostructuring of graphene grown on SiC, allowing the formation of periodic local defects (Prével *et al.*, 2011). Focused helium ion beam milling provides patterning of few-layers graphene at much finer scales than ebeam lithography can provide and without as much damage incurred as when gallium ions are used (Boden *et al.*, 2010). The HIM provides a helium ion probe with a size smaller than 0.7 nm which can be scanned across a sample in a pre-defined pattern to selectively remove areas by direct sputtering of the graphene material (Bell *et al.*, 2009). The helium ion beam also exhibits a low proximity

effect compared with an electron beam, thus allowing highly localised writing. Figure 14.2 shows (a) a nanobeam, (b) a wine glass disk resonator nanostructure and (c) a resonant torque nanostructure (Moktadir *et al.*, 2010). These structures were patterned with a resolution of 1 nm pixel^{-1} . After patterning, the structures were released by vapour HF etching of the underlying oxide (300 nm thick). The fine edges of these structures can be seen because of the very small spot of the beam. This level of detail is very hard to achieve with e-beam lithography, which is widely used for graphene patterning. In Fig 14.3, the nanobeam has a length of $1 \mu\text{m}$ and a width of about 200 nm, whereas the resonator has a diameter of $1 \mu\text{m}$ and a gap of less than 30 nm. Gaps less than 10 nm can be achieved. These structures are very familiar MEMS and NEMS structures that are used as sensors or



14.2 Helium ion patterning of nanostructures on bilayer graphene: (a) a nanobeam having length $1 \mu\text{m}$, width 200 nm; (b) a wine glass disk graphene resonator; and (c) a resonant torque structure.



14.3 The high-frequency mixing experimental setup used to measure the resonant frequency and the quality factor of graphene nanoresonators. (From Chen *et al.*, 2009, with permission.)

resonators. This technology is also promising for the fabrication of nanoelectronic devices. It can be used in combination with e-beam lithography such that features with a minimum size of a few tens of nanometres are patterned with ebeam lithography whereas sub 10nm features are patterned with the HIM (Hang *et al.*, 2013).

14.5 Graphene nanoresonators

Most of the current NEMS devices fabricated on graphene are nanoresonators. These are suspended graphene sheets made by etching of the silicon oxide sacrificial layer (Chen *et al.*, 2009) or by the transfer of graphene to a prepatterned substrate (Garcia-Sanchez *et al.*, 2008). These suspended beams or sheets are actuated either electrostatically or optically (Bunch *et al.*, 2007, van der Zande *et al.*, 2010) and their resonant frequencies and quality factors are measured. Understanding the behaviour of the atomically thin graphene resonators is an active area of research. Efforts are particularly directed to pinpoint the energy loss (damping) mechanisms on atomically thin graphene structures. Graphene resonators might find applications in radiofrequency, ultrasensitive mass sensing and quantum mechanical information processing. In the following subsections, we show how these devices are fabricated and describe the techniques used to measure their mechanical characteristics, i.e. resonant frequency and quality factor.

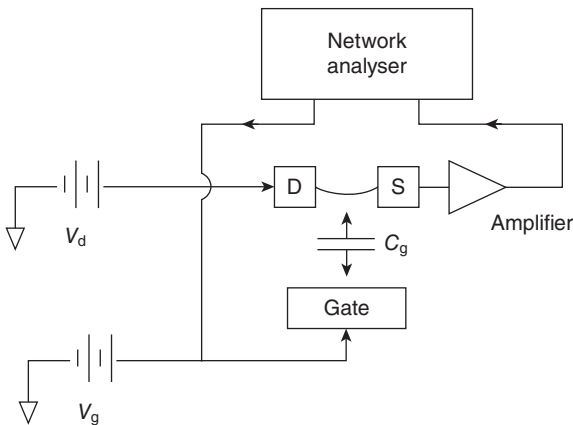
14.5.1 Fabrication techniques

In general, graphene suspended structures are fabricated by etching the underlying oxide using buffered hydrofluoric acid (BHF) or the transfer of graphene sheets to a substrate where trenches are pre-made (van der Zande *et al.*, 2010). In the first method, graphene layers are prepared by exfoliation of graphite and transferred to a substrate coated with 90 or 300nm of silicon oxide. In order to suspend the sheets, they have to be clamped in both ends. In this instance, electrical contacts are used as clamping pads. The contacts are made using ebeam lithography followed by a lift-off process, where a thin film of metal is deposited by evaporation. After contact deposition, the underlying oxide sacrificial layer is etched in BHF. In order to avoid the suspended structures sticking to the substrate, two methods are used: critical point drying (Bolotin *et al.*, 2008) and vapour HF etch (Moktadir, 2010). Structuring of graphene before suspension is also possible, for example for the fabrication of nanobeams resonators. In the second method, trenches are prepatterned onto the underlying oxide and contact electrodes are deposited; then exfoliated or CVD-grown graphene is transferred and suspended over the trenches (van der Zande *et al.*, 2010).

14.5.2 Characterisation techniques

To measure the resonant frequency and the quality factor of graphene resonators, optical and electrical methods are both used. One of the commonly used electrical measurement techniques is the high-frequency mixing approach (Chen *et al.*, 2009) developed to detect the motion of nanotubes resonators (Witkamp *et al.*, 2006). In this method, a dc gate voltage V_g applied to the device in combination with a radiofrequency gate voltage having a frequency f that drives the motion, i.e. $V = V_g + a\cos(2\pi ft)$. A second rf voltage, at a frequency $f + \Delta f$, is applied to the source ($\Delta f/f \ll 1$). During the motion of the resonator, its conductance changes with distance from the substrate and the motion is detected as a mixed-down current at the difference frequency Δf . This method is more suitable for monolayer structures because the conductivity response to the gate modulation is weak in multilayer graphene. A sketch of the measurement setup is shown in Fig 14.3.

However, the drawback of this technique is that it limits the measurements to a bandwidth of roughly 1 kHz (Chen *et al.*, 2009) making it unsuitable for broad rf applications. Xu *et al.* (2010) used another technique, where the stray capacitance is minimised and where direct readout on graphene resonators is performed using a network analyser. The circuit used to drive and detect the mechanical oscillation of the graphene resonator is shown in Fig 14.4, where a dc voltage V_d is applied to the drain. A rf signal with amplitude v_g and drive frequency f is combined with a dc voltage v_g and applied to the gate. Using a bias tee, the current is divided into dc and rf



14.4 Measurement setup using a network analyser, which allows direct readout on graphene resonators. (From Xu *et al.*, 2010, with permission.)

components; the latter is fed to a network analyser. The measured transmission of the device is $S_{12} = 50I_{rf}/v_g$, where I_{rf} is the rf component of the current.

Another method of characterisation of graphene resonators is the optical method, for example the method used by Bunch *et al.* (2007). The optical drive is performed using a laser diode with 432 nm wavelength. This signal is frequency-modulated using a network analyser and directly focused on the moveable graphene sheet. The graphene sheet and the underlying substrate form an interferometer that allows the detection of the vibrations by recording the reflected intensity from of the resonator using a second laser with a wavelength of 632.8 nm, focused on the suspended resonator. In recent work, Raman spectroscopy and Fizeau interferometry were used to detect mechanical resonances of graphene cantilevers (Reserbat-Plantey *et al.*, 2012). The advantage of this method is that it allows the resonators to be probed at sub-micrometre dimensions (few 100s of a nanometre). The multilayer cantilevers are clamped in one end to a gold film and form the upper mirror of an optical cavity having the underlying silicon oxide as its second mirror. The optical length of the cavity can thus be adjusted by electrostatic drive of the cantilever, resulting in the translation of the interference fringes pattern, which, in turn, allows the detection of motion. Raman spectroscopy was also used to detect the resonance frequency. Because the lifetime of optical phonons is (~ 1 ps) $\ll \tau_0 = \omega_0^{-1}$ (ω_0 being the resonance frequency), the scattered photons are detected instantaneously providing information about the stress in the moving cantilever (Reserbat-Plantey *et al.*, 2012).

14.5.3 Vibration spectrum

Depending on the shape, size and number of layers, the resonant frequency of graphene nanoresonators can vary from a few MHz to hundreds of MHz. The fundamental frequency of a vibrating beam is given by Stoney (1988):

$$f_0 = \frac{(\lambda)^2}{2\pi} \frac{1}{L^2} \sqrt{\frac{EI}{\rho A}} \quad [14.3]$$

where $\lambda = 4.73$; E , ρ , A , I are the Young modulus, mass density, cross-section area of the beam and the area moment of inertia of the cross-section, respectively. If the beam is under a small tension T then a second term is added to the equation above (Sapmaz *et al.*, 2003):

$$f_0 = \frac{(\lambda)^2}{2\pi} \frac{1}{L^2} \sqrt{\frac{EI}{\rho A}} + \frac{0.28}{2\pi} T \sqrt{\frac{1}{\rho A EI}} \quad [14.4]$$

For a beam with a constant cross-section and length L , width w and thickness t , the moment I is given by:

$$I = \frac{wh^3}{12} \quad [14.5]$$

where w and h are the width and the height of the beam, respectively. The vibration spectrum is determined by sweeping the excitation frequency. In general, and in linear response, the vibration spectrum fits well with a Lorentzian, allowing the determination of various parameters. In Fig. 14.5(a), a spectrum of a clamped–clamped monolayer graphene beam of length $L = 2\ \mu\text{m}$ and width $W = 3\ \mu\text{m}$ is shown (van der Zande *et al.*, 2010). The suspended beam was obtained by patterning graphene grown by CVD on a copper foil; the patterned graphene is then transferred into a silicon oxide substrate which was prepatterned onto trenches. This spectrum is obtained by the optical method described above. The resonant frequency of monolayer graphene depends on the physical state of the beam i.e. strain and the absorbed mass (which can result from contamination during processing). The resonant frequency can be modelled by the expression (van der Zande *et al.*, 2010):

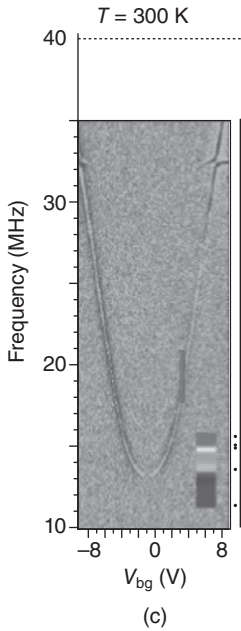
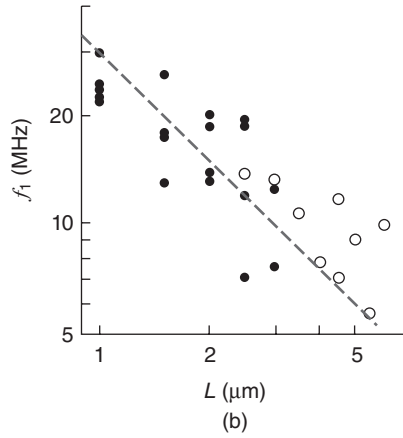
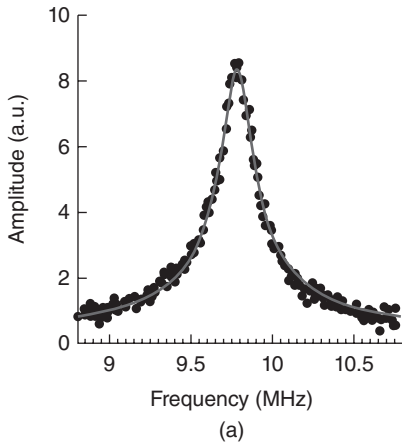
$$f_k = \frac{k}{2} \sqrt{\frac{E}{\rho_0 L^2}} \sqrt{\frac{s}{\alpha}} \quad [14.6]$$

where E and ρ_0 are the Young modulus and the mass density of monolayer graphene, respectively; $k = 1, 2, \dots$. The quantity s is the in-plane strain and α is the absorbed mass factor, i.e. $\alpha = \rho/\rho_0$ is the density including the absorbed mass. Equation [14.6] indicates a $1/L$ -dependence on the natural frequency of monolayer graphene, which is confirmed experimentally as shown in Fig 14.5(b).

The resonant frequency of monolayer graphene resonator also depends on the gate voltage (van der Zande *et al.*, 2010). Figure 14.5(c) shows this dependence at $T = 30\ \text{K}$. In these measurements, the current mixing method described earlier was used. The resonant frequency increases by a factor of two when the back gate voltage is swept from 0 to 8V. An interesting observation is that the resonant frequency dependence on the gate voltage becomes weak at low temperature. Although *a priori* this weak dependence can be attributed to the change in tension in graphene under cooling, it remains poorly understood and this dependence on tension as the resonator is cooled down is not yet quantified. A similar trend was observed in exfoliated graphene by Chen *et al.* (2009), where the effect of the added mass was investigated.

14.5.4 Quality factor

Measurements show that the quality factor of graphene resonators is rather low compared with that of other semiconductor resonators, because of the



14.5 (a) Spectrum of a monolayer graphene beam with dimensions $L = 2\mu\text{m}$ and $w = 3\mu\text{m}$, showing a resonance frequency at $f_0 = 9.77\text{MHz}$. (b) $1/L$ -dependence of the first-resonant mode frequency on the length of the monolayer graphene beam resonator. (c) Map of the mixing current, showing the resonant frequency variation as a function of the gate voltage. (From van der Zande *et al.*, 2010, with permission.)

large energy dissipation in graphene resonators, caused by a variety of dissipation mechanisms, which are not fully understood. Theoretically, several mechanisms were suggested (Seoáñez *et al.*, 2007). These are listed in Table 14.2 for an ideal graphene sheet, where the temperature dependence (T) is also shown. It is noticed that when there is a T -dependence, it is linear to the inverse of the quality factor Q^{-1} . Seoáñez *et al.* (2007) suggested that at high temperatures, ohmic loss in the metallic gate and the graphene sheet is the dominant dissipation mechanism. In this case, the inverse of the quality factor has a quadratic dependence on the total charge of the graphene sheet. The latter is readily controllable by the gate voltage. At low temperatures, attachment losses (a process where energy is irradiated away from the resonator) can play an important role in the dissipative process. Another cause of dissipation is the coupling of the resonator to a ‘two level system’ (Seoáñez *et al.*, 2007). Two-level systems are atoms or a group of atoms residing in the gate dielectric (i.e. SiO_2) and having two degenerate energy configurations. They interact with vibrations causing transitions between the two energy levels. The dissipation in this instance is caused by the coupling between the vibrating graphene sheet and these systems. If the sheet is strongly driven, then the dissipation can be significant.

Experimentally, the quality factor varies from a few thousands at low temperature to a few hundreds at room temperature (Bunch *et al.*, 2007, Chen *et al.*, 2009, van der Zande *et al.*, 2010, Barton *et al.*, 2011). These values are rather small compared with the theoretical predictions of Seoáñez *et al.* (2007). This is because, experimentally, graphene is far from an ideal crystal, as processing, rippling and impurities are all factors contributing to energy dissipation. The quality factor decreases with the increasing electrostatic force used to actuate the resonator (through the back gate actuation in a typical resonator). Electrostatic force induces softening of the spring constant of the vibrating resonator. This causes the resonator to be closer

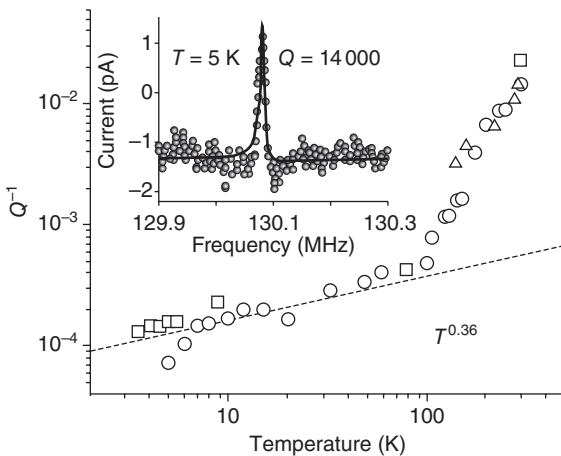
Table 14.2 Temperature dependence of the inverse of quality factor of a graphene resonator beam as a function of the dissipation mechanism involved (from Seoáñez *et al.*, 2007, with permission)

	Temperature-dependence of Q^{-1} (T)
Charges in SiO_2	T
Charges in graphene	T
Sheet and metallic gate	
Breaking and healing of surface bonds	–
Two level systems	$A + BT$
Attachment losses	–
Thermoelastic losses	T

to the substrate resulting in a large dissipation (Singh *et al.*, 2010). The quality factor decreases with the gate voltage and shows a dip at the Dirac point (corresponding to the minimum conductivity in the graphene sheet), the dip in the quality factor may be explained by ohmic losses, because the resistance of the graphene resonator is at its maximum at the Dirac point.

An example of temperature dependence of the quality factor is shown in Fig. 14.6 (Chen *et al.*, 2009). Here, the resonators are made of monolayer graphene and clamped on both ends. The quality factor reached a value of 14000 at 5 K. These measurements show a lack of tunability (by means of the gate voltage) of the resonator frequency at low temperature. The inverse of the quality factor Q^{-1} shows a power law dependence on temperature with an exponent $\alpha = 0.36$. The power law dependence on T is still not explained.

Graphene nanoresonators can also show nonlinear resonance phenomena (Chen *et al.*, 2009, Eichler *et al.*, 2011), where the vibration spectrum is no longer a Lorentzian. In general, the damping process is linear, varies proportionally with the speed and is independent of the amplitude. Eichler *et al.* (2011) investigated graphene and carbon nanotube resonant structures and found a strong nonlinear damping in those structures. They also found that the quality factor was strongly dependent on the vibration amplitude. They considered three types of resonators: graphene under tensile stress, carbon nanotubes under tensile stress and carbon nanotubes under slack. The dynamics of these resonators were described by the following differential equation:



14.6 Temperature dependence of the inverse of the quality factor for monolayer graphene resonators. The inset shows the vibration spectrum at $T = 5\text{ K}$ with a quality factor of 14000. (From Chen *et al.*, 2009, with permission.)

$$m \frac{d^2 x}{dt^2} = -kx - \gamma \frac{dx}{dt} - \alpha x^3 - \eta x^2 \frac{dx}{dt} + A \cos(2\pi ft) \quad [14.7]$$

where A is the excitation amplitude, k the spring constant, γ the linear damping coefficient, α the Duffing nonlinear coefficient and η the nonlinear damping coefficient. Eichler *et al.* achieved a quality factor of 100 000 at 90 mK, the highest recorded so far in graphene resonators.

14.6 Graphene nanomechanical sensors

In recent years there has been an extensive interest in graphene biosensors thanks to their sensitivity to external conditions and their field-effect tuning properties. The principal of sensing in graphene biosensors is based on electronic exchange between the adsorbed biological species and the graphene field-effect channel. This interaction leads to a change in resistance in the channel and this can be detected. For instance, graphene sensors were used to detect proteins, glucose and gas molecules (Ohno *et al.*, 2009, Wu *et al.*, 2009, Alwarappan *et al.*, 2009). These sensors exploit the very high values of the mobility in monolayer graphene because the detection sensitivity depends on transconductance of the graphene field-effect channel.

14.6.1 Biosensing membranes

Perhaps the most outstanding application of suspended graphene membranes in biology is the detection of DNA (Garaj *et al.*, 2010). Here a nanopore is drilled on a graphene layer separating two chambers containing ionic solutions. The ionic current flowing between the two chambers is measured as a DNA molecule is translocated through the nanopore. Graphene membranes were mounted on silicon nitride membranes with apertures separating two ionic solutions in contact with Ag/AgCl electrodes. The ionic current is reduced or blocked as the DNA molecule translocates through the pores. This gives an idea of the size of the molecule and its conformation (Garaj *et al.*, 2010).

Nanopores made on a layered structure made of alternating graphene and Al_2O_3 were also used to sense DNA and DNA-protein complexes (Venkatesan *et al.*, 2012). The multilayer structure was termed nanolaminate membrane where a nanopore was drilled using an electron beam. The advantage of such structure is the low electrical noise and high sensitivity to electrolytes having very low pH. This sensor is a three-terminal nanopore device which allowed very high temporal resolution sensing of folded and unfolded DNA molecules and RecA-coated DNA.

14.6.2 Graphene-based mass sensors

When a small amount of mass δm is added to a resonating nanobeam, a shift in its resonance frequency is observed. To obtain this frequency shift, Rayleigh approximation is used: the beam is treated as a harmonic oscillator with a mass m and a stiffness k . The equivalent mass and the stiffness are given by the following two relations (Stokey, 1988):

$$m = \int_0^L \rho A \phi(x)^2 dx \quad [14.8]$$

$$k = \int_0^L EI(\phi(x)''')^2 dx \quad [14.9]$$

where $\phi(x)$ is a shape function satisfying the beam differential equation and the appropriate boundary condition; ρ , E , I and A are the mass density of the beam, the Young modulus, the area moment of inertia and the beam cross-section, respectively. If we neglect the electrostatic spring softening (which is introduced during electrostatic actuation) and assume that the added mass does not change the spring constant of the beam, then the approximate resonant frequency is given by:

$$f_0 = \frac{\sqrt{k}}{2\pi} \frac{1}{\sqrt{m}} \quad [14.10]$$

Therefore we are able to calculate the resonance frequency shift δf for a small variation of mass δm :

$$\begin{aligned} \delta f &= f_0 - f' = f_0 \left(1 - \frac{1}{\sqrt{1 + \frac{\delta m}{m}}} \right) \\ &\approx f_0 \frac{\delta m}{2m} = R \delta m \quad (\delta m \ll m) \end{aligned} \quad [14.11]$$

where the responsivity R is defined as $f_0/2m$. Thus, in order to increase the responsivity beams, a small mass and a high resonant frequency are desired. This requirement can be achieved with nanotubes as their mass is extremely low ($\sim 10^{-21}$ kg) and their mechanical properties allow for very high resonant frequencies. Indeed Jensen *et al.* (2008) fabricated carbon nanotube mass sensors which achieved atomic resolution i.e. a responsivity of $0.104 \text{ MHz zg}^{-1}$ which corresponds to few tens of gold atoms. Also, these devices showed a sensitivity of $0.4 \text{ gold atoms/Hz}^{1/2}$ which is strikingly extremely low considering that the measurements are performed at room temperature. In this study, beams clamped at one end were used as their travel range when bent is larger than the travel range of clamped-clamped beams, allowing increased dynamic range. Another advantage of using cantilevers is that the loss owing to clamping is less than with doubly clamped ones.

Graphene nanoribbons or nanosheets can fulfil the above requirements, provided that the fabricated devices have a high quality factor at room temperature. So far, high-quality factors for graphene resonators have only been obtained at low temperatures.

14.7 Conclusion and future trends

Graphene nanoelectromechanical systems show a promising future considering that graphene was only recently discovered. Significant progress has been made in graphene nanoscale fabrication allowing the development of atomically thin devices which have the possibility to take NEMS beyond what other NEMS materials have achieved. Graphene has remarkable electronic properties and, if combined with nanoscale moveable structures, could allow the development of devices that can interact with single atoms. Carbon nanotubes also have great potential and show extraordinary mechanical properties. However, their integration and control over their location on-chip make the mass production of carbon nanotube-based NEMS devices difficult to achieve. On the contrary, graphene can be produced on a wafer scale using CVD or SiC annealing and significant progress has been made in this direction. In addition, graphene processing is compatible with other top-down processing techniques making its integration with other components possible. Hybrid graphene structures combining purely electronic devices with mechanical motion present us with exciting possibilities. For example, one can explore the interaction between single electron phenomena on suspended graphene quantum dots, use vibration modes to explore and harness quantum phenomena, and build enhanced sensors for beyond CMOS era. Interfacing biofunctionalised graphene nanoresonators and atomically thin membranes will allow the fabrication of a variety of biodevices used in several biotechnological applications.

Graphene NEMS have a good future and research worldwide is underway to explore the possibilities offered by this material.

14.8 References

- Abele N., Fritschi R., Boucart K., Casset F., Ancey P. and Ionescu A. M. (2005) Suspended-gate MOSFET: bringing new MEMS functionality into solid-state MOS transistor, IEEE Electron Devices Meeting, 2005. *IEDM Technical Digest* 479–481.
- Alwarappan S., Erdem A., Liu, C. and Li C.-Z. (2009) ‘Probing the electrochemical properties of graphene nanosheets for biosensing applications’, *J. Phys. Chem. C* **113**, 8853–8857.
- Atalaya J., Isacsson A. and Kinaret J. M. (2008) ‘Continuum elastic modelling of graphene resonators’, *Nano Lett.* **8**(12), 4196–4200.

- Balandin A. A., Ghosh S., Bao W., Calizo I., Teweldebrhan D., Miao F. and Lau C. N. (2008), 'Superior thermal conductivity of single-layer graphene', *Nano Lett.* **8**(3), 902–907.
- Barton R. A., Parpia J. and Craighead H. G. (2011) 'Fabrication and performance of graphene nanoelectromechanical systems', *J. Vac. Sci. Technol. B* **29**, 050801.
- Bell D. C., Lemme M. C., Stern L. A., Williams J. R. and Marcus C. M. (2009) Precision cutting and patterning of graphene with helium ions, *Nanotechnology* **20**, 455301.
- Blakslee O. L., Proctor D. G., Seldin E. J., Spence G. B., Weng T. (1970) *J. Appl. Phys.* **41**, 3373.
- Boden S., Mokhtadir Z., Bagnall D., Mizuta H. and Rutt, H. (2010) 'Focused helium ion beam milling and deposition', *Microelectron. Eng.* **88**, 2452–2455.
- Bolotin K. I., Sikes K. J., Jianga Z., Klima M., Fudenberg G., Hone J., Kim P., Stormer H. L. (2008) 'Ultrahigh electron mobility in suspended graphene', *Solid State Commun.* **146**, 351–355.
- Buks E. and Roukes M. L. (2001) 'Stiction, adhesion energy, and the Casimir effect in micromechanical systems', *Phys. Rev. B* **63**, 033402.
- Bunch J. S., van der Zande A. M., Verbridge S. S., Frank I. W., Tanenbaum D. M., Parpia J. M., Craighead H. G., McEuen P. L. (2007) 'Electromechanical resonators from graphene sheets', *Science* **315**, 490.
- Bunch J. S., Verbridge S. S., Alden J. S., van der Zande A. M., Parpia J. M., Craighead H. G. and McEuen P. L. (2008) 'Impermeable atomic membranes from graphene sheets' *Nano Lett.* **8**(8), 2458–2462.
- Cadelano E., Palla P. L., Giordano S. and Colombo L. (2009) 'Nonlinear elasticity of monolayer graphene', *Phys. Rev. Lett.* **102**, 235502.
- Chen C., Rosenblatt S., Bolotin K. I., Kalb W., Kim P., Kymissis I., Stormer H. L., Heinz T. F. and Hone J. (2009) *Nat. Nanotechnol.* **4**, 861–867.
- de Heer W. A., Berger C., Wu X., First P. N., Conrad E. H., Li X., Li T., Sprinkle M., Hass J., Sadowski M. L., Potemski M., Martinez G. (2007) 'Epitaxial graphene' *Solid State Commun.* **143**, 92–100.
- Delhaes P (2001) *Graphite and precursors*. CRC Press. ISBN 90-5699-228-7.
- Dual J., Mazza E., Schiltges G. and Schlums D. (1997) 'Mechanical properties of microstructures: experiments and theory', *Proc. SPIE* **3225**, 12–22.
- Eichler A., Moser J., Chaste J., Zdrojek M., Wilson-Rae I. and Bachtold A. (2011) 'Nonlinear damping in mechanical resonators made from carbon nanotubes and graphene', *Nat. Nanotechnol.* **6**, 339–342.
- Emtsev K. V., Bostwick A., Horn K., Jobst J., Kellogg G. L., Ley L., McChesney J. L., Ohta T., Reshanov S. A., Röhrl J., Rotenberg E., Schmid A. K., Waldmann D., Weber H. B. and Seyller T. (2009) 'Towards wafer-size graphene layers by atmospheric pressure graphitization of silicon carbide', *Nat. Mater.* **8**, 203–207.
- Fasolino A., Los J. H. and Katsnelson M. I. (2007) 'Intrinsic ripples in graphene'. *Nat. Mater.* **6**(11), 858–861.
- Gad-el-Hak M. (2002) editor, *MEMS Handbook*, CRC press.
- Garaj S., Hubbard W., Reina A., Kong J., Branton D. and Golovchenko J. A. (2010) 'Graphene as a subnanometre trans-electrode membrane', *Nature* **467**, 190–193.
- Garcia-Ramirez M. A., Tsuchiya Y. and Mizuta H. (2010) 'Hybrid circuit analysis of a suspended gate silicon nanodot memory (SGSNM) cell', *Microelectron. Eng.* **87**, 1284–1286.

- Garcia-Sanchez D., van der Zande A. M., San Paulo A., Lassagne B., McEuen P. L. and Bachtold A. (2008) 'Imaging mechanical vibrations in suspended graphene sheets', *Nano Lett.* **8**(5), 1399–1403.
- Hang S., Muktadir Z. and Mizuta H. (2013) 'Ultra-fine graphene nanoelectronic devices carved with tightly focused helium ion beam', The 7th international conference on the fundamental science of graphene and applications of graphene-based devices (Graphene Week 2013), Chemnitz, DE.
- Hass J., Jeffrey C. A., Feng R., Li T., Li X., Song Z., Berger C., de Heer W. A., First P. N., Conrad H. E. (2006) 'Highly ordered graphene for two dimensional electronics', *Appl. Phys. Lett.* **89**, 143106.
- Huang P. Y., Ruiz-Vargas C. S., van der Zande A. M., Whitney W. S. Levendorf Mark P., Kevek J. W., Garg S., Alden J. S., Hustedt C. J., Zhu Y., Park J., McEuen P. L. and Muller D. A. (2011) 'Grains and grain boundaries in single-layer graphene atomic patchwork quilts', *Nature* **469**, 389–392.
- Ishigami M., Chen J. H., Cullen W. G., Fuhrer M. S. and Williams E. D. (2007) 'Atomic structure of graphene on SiO₂', *Nano Lett.* **7**(6), 1643–1648.
- Jensen K., Kim K. and Zettl A. (2008) 'An atomic-resolution nanomechanical mass sensor' *Nat. Nanotechnol.* **3**, 533–537.
- Jiang J.-W., Wang J.-S. and Li B. (2009) 'Young's modulus of graphene: a molecular dynamics study', *Phys. Rev. B* **80**, 113405.
- Kim K., Choi J.-Y., Kim T., Cho S.-H. and Chung H.-J. (2011) 'A role for graphene in silicon-based semiconductor devices', *Nature* **479**, 338–344.
- Kim K. S., Zhao Y., Houk J., Lee S. Y., Kim J. M., Kim K. S., Jong-Hyun Ahn, Kim P., Choi J.-Y. and Hong B. H. (2009) *Nature* **457**, 706–710.
- Lee C., Wei X., Kysar J. W. and Hone J. (2008) 'Measurement of the elastic properties and intrinsic strength of monolayer graphene', *Science* **321**, 385–388.
- Lee K. M., Neogi A., Perez J. M. and Choi T. Y. (2010) 'Focused-ion-beam-assisted selective control of graphene layers: acquisition of clean-cut ultra-thin graphitic film', *Nanotechnology* **21**, 205303.
- Lee Y., Bae S., Jang H., Jang S., Zhu S. E., Sim S. H., Song Y. I., Hong B. H. and Ahn J.-H. (2010) 'Wafer-scale synthesis and transfer of graphene films' *Nano Lett.* **10**, 490–493.
- Li X., Cai W., An J., Kim S., Nah J., Yan D., Piner R., Velamakanni A., Jung I., Tutuc E., Banerjee S. K., Colombo L. and Ruoff R. S. (2009a) 'Large-area synthesis of high-quality and uniform graphene films on copper foils', *Science* **324**, 1312.
- Li X., Zhu Y., Cai W., Borysiak M., Han B., Chen D., Piner R. D., Colombo L. and Ruoff R. S. (2009b) 'Transfer of large-area graphene films for high-performance transparent conductive electrode' *Nano Lett.* **9**(12), 4359–4363.
- Lin Y.-C., Lu C.-C., Yeh C.-H., Jin C., Suenaga K. and Chiu P. W. (2012) 'Graphene annealing: how clean can it be?' *Nano Lett.* **12**(1), 414–419
- Liu F., Ming P. and Li J. (2007) 'Ab initio calculation of ideal strength and phonon instability of graphene under tension' *Phys. Rev. B* **76**, 064120.
- Marszalek P. E., Greenleaf W. J., Li H., Oberhauser A. F. and Fernandez J. M. (2000) 'Atomic force microscopy captures quantized plastic deformation in gold nanowires'. *Proc. Nat. Acad. Sci.* **97**, 6282–6286.
- Meyer J. C., Geim A. K., Katsnelson M. I., Novoselov K. S., Booth T. J. and Roth S. (2007) 'The structure of suspended graphene sheets' *Nature* **446**, 60–63.

- Moktadir Z., Boden S., Mizuta H. and Rutt H. (2010) 'Graphene for nano-electromechanical systems', *MME2010: 21st Micromechanics and Micro systems Europe Workshop*, Enschede, The Netherlands, p. 88.
- Norton P., Braggins T. and Levinstein H. (1973) 'Impurity and lattice scattering parameters as determined from Hall and mobility analysis in n-type silicon', *Phys. Rev. B* **8**, 5632–5653.
- Novoselov K. S., Geim A. K., Morozov S. V., Jiang D., Katsnelson M. I., Grigorieva I. V., Dubonos S. V. and Firsov A. A. (2005) 'Two-dimensional gas of massless Dirac fermions in graphene' *Nature* **438**, 197–200.
- Novoselov K. S., Geim A. K., Morozov S. V., Jiang D., Zhang Y., Dubonos S. V., Grigorieva I. V. and Firsov A. A. (2004) 'Electric field effect in atomically thin carbon films', *Science* **306**, 666.
- Obraztsov A. N., Obraztsova E. A., Tyurnina A. V. and Zolotukhin A. A. (2007) 'Chemical vapour deposition of thin graphite films of nanometer thickness', *Carbon* **45**, 2017.
- Ohno Y., Maehashi K., Yamashiro Y. and Matsumoto K. (2009) 'Electrolyte-Gated graphene field-effect transistors for detecting pH and protein adsorption', *Nano Lett.* **9**(9), 3318–3322.
- Prével B., Benoit J. M., Bardotti L., Mélinon P., Ouerghi A., Lucot D., Bourhis E. and Gierak J. (2011) 'Nanostructuring graphene on SiC by focused ion beam: effect of the ion fluence' *Appl. Phys. Lett.* **99**, 083116
- Qian D., Wagner G. J., Liu W. K., Yu M. F. and Ruoff R. S. (2002) 'Mechanics of carbon nanotubes' *Appl. Mech. Rev.* **55**, 495.
- Reserbat-Plantey A., Marty L., Arcizet O., Bendiab N. and Bouchiat V. (2012) 'A local optical probe for measuring motion and stress in a nanoelectromechanical system', *Nat. Nanotechnol.* **7**, 151–155.
- Reyntjens S. and Puers R. (2001) 'A review of focused ion beam applications in microsystem technology', *J. Micromech. Microeng.* **11**, 287–300.
- Sapmaz S., Blanter Y. M., Gurevich L. and van der Zant H. S. J. (2003) 'Carbon nanotubes as nanoelectromechanical systems', *Phys. Rev. B* **67**, 235414.
- Sato K., Yoshioka T., Ando T., Shikida M. and Kawabata T. (1998) 'Tensile testing of silicon film having different crystallographic orientations carried out on a silicon chip', *Sensors and Actuators A: Physical* **70**, 148–152.
- Seoáñez C., Guinea F. and Castro Neto A. H. (2007) 'Dissipation in graphene and nanotube resonators' *Phys. Rev. B* **76**, 125427.
- Singh V., Sengupta S., S Solanki H., Dhall R., Allain A., Dhara S., Pant P. and Deshmukh M. M. (2010) 'Probing thermal expansion of graphene and modal dispersion at low-temperature using graphene nanoelectromechanical systems resonators', *Nanotechnology* **21**, 165204.
- Stokey W. (1988) 'Vibration of systems having distributed mass and elasticity' in *Shock and vibration handbook*, 4th edition edited by C. Harris, McGraw-Hill, New York.
- Tanaka M., Higashida K. and Haraguchi T. (2004) 'Microstructure of plastic zones around crack tips in silicon revealed by HVEM and AFM', *Mater. Sci. Eng. A*, 387–389, 433–437.
- Tsuchiya T., Hirata M., Chiba N., Udo R., Yoshitomi Y., Ando T., Sato K., Takashima K., Higo Y., Satomae Y., Ogawa H. and Ozaki K. (2005) 'Cross comparison of thin-film tensile-testing methods examined using single-crystal silicon, polysilicon, nickel, and titanium films', *J. Microelectromechanical Systems* **14-5**, 1178–1186.

- van der Zande A. M., Barton R. A., Alden J. S., Ruiz-Vargas C. S., Whitney W. S., Pham P. H. Q., Park J., Parpia J. M., Craighead H. G. and McEuen P. L. (2010) 'Large-scale arrays of single-layer graphene resonators', *Nano Lett.* **10**(12), 4869–4873.
- Venkatesan B. M., Estrada D., Banerjee S., Jin X., Vincent E., Dorgan V. E., Bae M.-H., Aluru N. R., Pop E. and Bashir R. (2012) 'Stacked graphene- Al_2O_3 nanopore sensors for sensitive detection of DNA and DNA-Protein complexes', *ACS Nano* **6**(1), 441–450.
- Wang C., Morton K. J., Fu Z., Li W.-D. and Chou S. Y. (2011) 'Printing of sub-20 nm wide graphene ribbon arrays using nanoimprinted graphite stamps and electrostatic force assisted bonding', *Nanotechnology* **22**, 445301.
- Wei X., Fregneaud B., Marianetti C. A. and Kysar J. W. (2009) 'Nonlinear elastic behavior of graphene: ab initio calculations to continuum description', *Phys. Rev. B* **80**, 205407.
- Witkamp B., Poot M. and van der Zant H. S. J. (2006) 'Bending-mode vibration of a suspended nanotube resonator', *Nano Lett.* **6**, 2904–2908.
- Wong E., Sheehan P. and Lieber C. (1997) 'Nanobeam mechanics: elasticity, strength, and toughness of nanorods and nanotubes', *Science* **277**, 1971–1975.
- Wu H., Wang J., Kang X., Wang C., Wang D., Liu J., Aksay I. A. and Lin Y. (2009) 'Glucose biosensor based on immobilization of glucose oxidase in platinum nanoparticles/graphene/chitosan nanocomposite film', *Talanta* **80**, 403–406.
- Xu Y., Chen C., Deshpande V. V., DiRenno F. A., Gondarenko A., Heinz D. B., Liu S., Kim P. and Hone J. (2010) 'Radio frequency electrical transduction of graphene mechanical resonators' *Appl. Phys. Lett.* **97**, 243111.
- Yoshishige T., Takai K., Momo N., Nagami T., Mizuta H., Oda S., Yamaguchi S. and Shimada T. (2006) 'Nanoelectromechanical nonvolatile memory device incorporating nanocrystalline Si dots', *J. Appl. Phys.* **100**, 094306.
- Yu M.-F., Lourie O., Dyer M. J., Moloni K., Kelly T. F. and Ruoff R. S. (2000) 'Strength and breaking mechanism of multiwalled carbon nanotubes under tensile load', *Science* **287**, 637.